Theoretical study of odd-mass Fr isotopes using the collective clusterization approach of the dynamical cluster-decay model

Gudveen Sawhney,[1] Gurvinder Kaur,[2] Manoj K. Sharma,[2,*] and Raj K. Gupta[1]
[1]*Department of Physics, Panjab University, Chandigarh 160014, India*
[2]*School of Physics and Materials Science, Thapar University, Patiala 147004, India*
(Received 5 August 2013; published 9 September 2013)

The reaction dynamics of various odd-mass Fr isotopes is studied over a wide range of incident energies, spread across the Coulomb barrier. The specific reactions analyzed are $^{18}O + ^{197}Au$ and $^{19}F + ^{192,194,196,198,200}Pt$, forming odd-mass $^{211-219}Fr^*$ compound systems where some data are available for three of these isotopes: $^{213,215,217}Fr^*$. Based on the dynamical cluster-decay model (DCM), we have extended our calculations of the evaporation residue (ER) cross sections to the mainly fissioning $^{215}Fr^*$, using the systematics of $^{213,217}Fr^*$ isotopes where the available ER cross sections (as well as fusion-fission cross sections) were studied earlier within the DCM. In order to obtain a clear picture of the dynamics involved, including entrance channel effects, the variations of fragmentation potential, preformation factor, and decay barrier height are analyzed. The relevance of barrier modification effects is also explored in the decay of $^{213,215,217}Fr^*$ nuclei. In addition, fusion-fission (ff) cross sections are extended to $^{213,217}Fr^*$ systems where some more data has recently become available. Also, the fission fragment anisotropies (so far measured and studied for $^{215}Fr^*$ alone) are estimated for $^{213,217}Fr^*$ using DCM for the use of nonsticking moment of inertia, and relevant comparison with the sticking moment-of-inertia approach is analyzed. Furthermore, the shell closure effects of the decay fragments are investigated for odd-mass $^{211-219}Fr^*$ isotopes.

DOI: 10.1103/PhysRevC.88.034603 PACS number(s): 25.70.Jj, 23.70.+j, 24.10.−i

I. INTRODUCTION

In heavy-ion fusion reactions, the compound nucleus (CN) is formed at a particular excitation energy (E^*_{CN}) with a broad range of angular momentum from $\ell = 0$ to ℓ_{max}. It is generally believed that decay of CN is independent of its mode of formation, except for the requirement of various conservation laws, and it can decay in a number of ways depending on the incident energy of the projectile and the deformations and shape orientations of both projectile and target nuclei. In general, the decay of CN goes through processes like the evaporation residue (ER), intermediate mass fragments (IMF), and fusion-fission (ff), described by various theoretical models, like the statistical evaporation [1–5] and fission model [6,7], the thermodynamical Dubna model of heated CN [8–10], and the dynamical cluster-decay model of Gupta and collaborators [11–22] used here. The ER consists of the light particles (LPs), neutrons, protons, α particles, and γ rays ($A \leqslant 4$), whereas IMFs are nuclei with masses $5 \leqslant A \leqslant 20$ and $2 \leqslant Z \leqslant 10$ and ff comprises the near-symmetric and symmetric fission fragments, nSF and SF. The IMFs could also be included in the ff process. Interestingly, different combinations of the above mentioned decay processes are found to occur in different mass regions of compound nuclei or any one of them as a dominant decay mode.

For Fr nuclei, we have recently studied [21,22] the odd-mass nuclear systems $^{213,215,217}Fr^*$ over a wide center-of-mass (c.m.) energy range of 48 to 94 MeV, using the DCM with deformation and orientation effects included in it. In DCM, we consider all the decay products (ER, IMF, and ff) as dynamical mass motion of preformed fragments or clusters through the interaction barrier, thereby including explicitly the structure effects of CN. For the measured decay paths of compound systems $^{213,217}Fr^*$, formed in $^{19}F + ^{194,198}Pt$ reactions at $E_{c.m.} = 80$–94 MeV [23], the fission anisotropy data for $^{217}Fr^*$ (with neutron number $N = 130$) shows a nice comparison with the statistical saddle-point model (SSPM), but the same is not true for $^{213}Fr^*$ (with $N = 126$), showing significant deviations between measured and SSPM calculated anisotropies. This anomaly in fission anisotropy for $^{213}Fr^*$ is believed by the authors [23] to be associated with either the magic $N = 126$ shell of the CN or a presence of a non-compound-nucleus (nCN) component, like the quasifission (qf), in fission cross section. On the other hand, our DCM calculated [21] ff cross sections (as well as the ER cross sections) match the available data [23] on both ER and ff, nearly exactly, with qf contribution of only ∼4–10% of ff cross sections (for the lowest to highest energy) for $^{213}Fr^*$ and 8–10% for $^{217}Fr^*$. However, the fission anisotropy data [23] itself was not analyzed on the DCM for $^{213,217}Fr^*$ systems, and the same is worked out in this paper. Note that the DCM is based on collective clusterization picture and, in DCM, the magic shell effects of CN do not come in to play. Instead, a small hump or shoulder is observed [21] in calculated fragment preformation yields, which arises due to deformed shell closure of light fragment $Z_2 = 36$ and spherical shell closure of heavy fragment $Z_1 = 50$, which is relatively more pronounced in the decay of $N = 126$ $^{213}Fr^*$ than in $N = 130$ $^{217}Fr^*$.

The decay of $^{215}Fr^*$ CN is studied within DCM [22] in reference to the older data of Ref. [24] where the CN is formed via two different reaction channels, $^{11}B + ^{204}Pb$ and $^{18}O + ^{197}Au$, at two different c.m. energy ranges of $E_{c.m.} = 47.97$–60.24 and 71.17–88.66 MeV, respectively. The chosen reaction channels have entrance-channel mass asymmetries lying on either side of the Bussinaro-Gallone

*msharma@thapar.edu

critical asymmetry parameter and hence are expected to have different preferences for pre-equilibrium fission or qf [25]. However, in agreement with experimental data and statistical model (PACE2) calculations, on both the ff cross sections and fission fragment anisotropies, the DCM confirms the entrance channel independence [22] of the decay of ^{215}Fr*. The role of sticking versus nonsticking moment of inertia is also analyzed for fixing the limiting angular momentum $\ell_{\max}$, since fission anisotropy supported the nonsticking limit $I_{\rm NS}$ and fusion-fission cross-section preferred the sticking limit $I_{\rm S}$.

In this paper, we extend our earlier works [21,22] of odd-mass ^{213,215,217}Fr* isotopes to a complete study of decay cross sections (both ER and ff) and fission fragment anisotropies for the reactions ^{18}O + ^{197}Au $\rightarrow$ ^{215}Fr* and ^{19}F + ^{194,198}Pt $\rightarrow$ ^{213,217}Fr* at the full range of $E_{\rm c.m.} = 48$–106 MeV, based on the three experiments of Refs. [23,24,26], using the collective clusterization approach of the DCM. The detailed analysis of temperature, angular momentum effects, preformation factor, barrier modification, etc., is worked out in the context of the reactions under investigation. In addition, the role of isospin (N/Z ratio of CN) is further explored for decay of Fr isotopes with mass number varying as $A = 211$–219; i.e., the above study extended to two other odd-mass isotopes ^{211,219}Fr*. The motivation of this study is to look for the possible role of shell effects of decaying fragments in the above mentioned Fr isotopes. Though shell effects of the compound nuclei as such play no role in the DCM, a comparison of the earlier studied potential energy surfaces for ^{213,217}Fr* with those of ^{211,215,219}Fr* isotopes could reveal the effects of the underlying shell closure in all the decaying Fr isotopes studied here.

The paper is organized as follows: A brief account of the DCM for a hot and rotating CN is given in Sec. II. The effects of deformations are included up to β_2, with "optimum" orientations $\theta^{\rm opt.}$ of two nuclei or fragments from Ref. [11]. The details of calculations and results obtained are presented in Sec. III. Finally, the conclusions drawn are summarized in Sec. IV.

II. THE MODEL

The DCM has been established for the study of heavy-ion reaction dynamics, whose detailed description can be found in Refs. [11–22]. In DCM, the decay cross section is defined in terms of the partial waves as

$$\sigma = \frac{\pi}{k^2}\sum_{\ell=0}^{\ell_{\max}}(2\ell+1)P_0P; \quad k=\sqrt{\frac{2\mu E_{\rm c.m.}}{\hbar^2}}, \tag{1}$$

which involves the collective coordinates of mass (and charge) asymmetry $\eta = (A_1 - A_2)/(A_1 + A_2)$ [and $\eta_Z = (Z_1 - Z_2)/(Z_1 + Z_2)$], the relative separation R to which are also added the multipole deformations $\beta_{\lambda i}$ ($\lambda = 2$, 3, 4) and orientations θ_i ($i = 1, 2$) of two outgoing nuclei or decay fragments (1 and 2 stand, respectively, for heavy and light fragments). Here, P_0 is the preformation probability, which refers to η motion and penetrability P to R motion. $\mu = [A_1A_2/(A_1 + A_2)]m$ is the reduced mass, with m as the nucleon mass. $\ell_{\max}$ is the maximum value of angular momentum where contribution to evaporation residue cross section reduces to zero [$\sigma_{\rm ER}(\ell) \rightarrow 0$ at $\ell = \ell_{\max}$]. The temperature (T) is related to CN excitation energy as

$$E^*_{CN} = (A_{\rm CN}/a)T^2 - T \tag{2}$$

with the level density parameter $a = 9$ for heavy compound systems.

Through the T-dependant liquid drop energy of Davidson *et al.* [27] and the "empirical" shell correction of Myers and Swiatecki [28], the fragmentation potential $V_R(\eta, T)$, at fixed R, used in stationary Schrödinger equation in η [Eq. (7) below] is defined in DCM as

$$\begin{aligned} V_R(\eta, T) = &\sum_{i=1}^{2}[V_{\rm LDM}(A_i, Z_i, T)] + \sum_{i=1}^{2}[\delta U_i]\exp\left(-T^2/T_0^2\right) \\ &+ V_C(R, Z_i, \beta_{\lambda i}, \theta_i, T) + V_P(R, A_i, \beta_{\lambda i}, \theta_i, T) \\ &+ V_\ell(R, A_i, \beta_{\lambda i}, \theta_i, T), \end{aligned} \tag{3}$$

where V_C, V_P, and V_ℓ are, respectively, the T-dependent Coulomb, nuclear proximity, and centrifugal potentials for deformed, oriented nuclei.

The T-dependent nuclear proximity potential V_P for deformed, oriented nuclei is

$$V_p(A_i, \beta_{\lambda i}, \theta_i, T) = 4\pi\bar{R}(T)\gamma b(T)\Phi[s_0(T)], \tag{4}$$

where $b(T) = 0.99(1 + 0.009T^2)$ is the nuclear surface thickness, $\gamma = 0.9517[1 - 1.7826(\frac{N-Z}{A})^2]$ MeV fm^{-2} is the surface energy constant, and $\overline{R}(T)$ is the mean curvature radius. $\Phi(s_0)$ in Eq. (4) is the universal function, independent of the shapes of nuclei or the geometry of nuclear system, but depends on the minimum separation distance $s_0(T)$. For details, see Ref. [29].

The centrifugal potential V_ℓ is obtained through the use of moment of inertia in the sticking limit $I_{\rm S} = \mu R^2 + \frac{2}{5}A_1mR_1^2(\alpha_1, T) + \frac{2}{5}A_2mR_2^2(\alpha_2, T)$, or alternatively, the one calculated in the nonsticking limit $I = I_{\rm NS} = \mu R^2$, given by

$$V_\ell(T) = \frac{\hbar^2\ell(\ell+1)}{2I(T)}. \tag{5}$$

It is relevant to note that $I_{\rm NS}$ is preferred [18,22] for fission anisotropy calculations, which can be further explored through the DCM within SSPM approach [6],

$$A = 1 + \langle\ell^2\rangle/4K_0^2, \tag{6}$$

where K_0^2 is the variance of the K distribution and $\langle\ell^2\rangle$ is the mean square angular momentum of the fissioning nucleus related to the total ℓ value (equivalently, $\ell_{\max}$ of the CN). Here, K_0^2 is related to the effective moment of inertia of the CN, $I_{\rm eff}$, and the saddle-point temperature T as

$$K_0^2 = T \times I_{\rm eff}/\hbar^2$$

with $I_{\rm eff}$ calculated by using the finite-range rotating liquid drop model [30], T being the temperature of the fissioning nucleus. The value of $\ell_{\max}$ depends on the use of $I_{\rm S}$ or $I_{\rm NS}$ in the centrifugal potential [Eq.(5)].

Using the fragmentation potential of Eq. (3), the stationary Schrödinger equation in η, at a fixed $R = R_a$, is

expressed as

$$\left\{-\frac{\hbar^2}{2\sqrt{B_{\eta\eta}}}\frac{\partial}{\partial\eta}\frac{1}{\sqrt{B_{\eta\eta}}}\frac{\partial}{\partial\eta}+V_R(\eta,T)\right\}\psi^{\nu}(\eta)=E^{\nu}\psi^{\nu}(\eta), \tag{7}$$

where $\nu = 0, 1, 2, 3, \ldots$, referring to ground-state ($\nu = 0$) and excited-state solutions. Solving the Schrödinger equation, we get the preformation probability P_0 in Eq. (1) as

$$P_0(A_i) = |\psi_R[\eta(A_i)]|^2\sqrt{B_{\eta\eta}}\frac{2}{A_{\rm CN}}. \tag{8}$$

The penetration probability P in Eq. (1) is calculated by using the WKB integral as

$$P = \exp\left[-\frac{2}{\hbar}\int_{R_a}^{R_b}\{2\mu[V(R)-Q_{\rm eff}]\}^{1/2}dR\right]. \tag{9}$$

For the decay of a hot CN, R_a, the first turning point of the penetration path(s) used for calculating the penetrability P, and the R value at which P_0 is calculated, is defined as

$$\begin{aligned} R_a &= R_1(\alpha_1,T)+R_2(\alpha_2,T)+\Delta R(T)\\ &= R_t(\alpha,T)+\Delta R(T), \end{aligned} \tag{10}$$

where ΔR is the relative separation distance between two fragments, shown to assimilate the neck formation effects and hence referred as the neck-length parameter. The radius vector R_i is given by

$$R_i(\alpha_i,T) = R_{0i}(T)\left[1+\sum_{\lambda}\beta_{\lambda i}Y_{\lambda}^{(0)}(\alpha_i)\right], \tag{11}$$

and T-dependent nuclear radii R_{0i} of the equivalent spherical nuclei [31],

$$R_{0i}(T) = \left[1.28A_i^{1/3}-0.76+0.8A_i^{-1/3}\right](1+0.0007T^2). \tag{12}$$

The neck-length parameter $\Delta R(T)$, in the definition of R_a above, allows us to define the effective barrier-lowering parameter $\Delta V_B(\ell)$ for each ℓ as the difference between the actually used barrier $V(R_a,\ell)$ and the top of the calculated barrier $V_B(\ell)$, as

$$\Delta V_B(\ell) = V(R_a,\ell)-V_B(\ell). \tag{13}$$

Notice that the actually used barrier is effectively lowered as the entry level R_a of penetration path is always lower than the barrier height V_B.

III. CALCULATIONS AND DISCUSSION

We have divided this section into two subsections. In Sec. III A, we present our calculations for the decay of ^{213,215,217}Fr* formed in reactions ^{19}F + ^{194}Pt, ^{18}O + ^{197}Au, and ^{19}F + ^{198}Pt, respectively, over a wide range of available incident energies [23,24,26]. It is important to note that the selected range of energies are above as well as below Coulomb barrier energy (the barrier lies around ∼84 MeV for ^{19}F + ^{194,198}Pt channels and 87 MeV for ^{18}O + ^{197}Au channel). Using the DCM, the yields of evaporation residues are predicted for the decay of ^{213,215,217}Fr* and fission data are addressed for ^{213,217}Fr* systems, at energies not covered in our earlier works [21,22]. Also, the channel independence of ^{18}O + ^{197}Au and ^{19}F + ^{196}Pt reactions is investigated and fission fragment anisotropies are calculated for the ^{19}F + ^{194,198}Pt reactions in addition to "barrier modification" effects at sub-barrier energies. Finally, in Sec. III B, the shell closure effects of the decay fragments and their N/Z dependence is explored for $^{211-219}$Fr* isotopes.

A. ER and ff excitation functions and fission anisotropies in decay of Fr isotopes

First of all, we look for the energetically favored light particles (LPs), the evaporation residue (ER), predicted by the DCM for the compound nucleus ^{215}Fr* formed in ^{18}O + ^{197}Au reaction and study their behavior with respect to angular momentum ℓ, and finally sum over ℓ up to $\ell_{\rm max}$. Since $\sigma_{\rm ER}$ are measured for ^{213,217}Fr* systems [23] but not for ^{215}Fr* [24], calculations are made within the DCM by using different neck-length parameters ΔR at different $E_{\rm c.m.}$ (equivalently, $E^*_{\rm CN}$ or T values), assuming that ΔR for the case of ^{215}Fr* lies in between that for the ^{213}Fr* and ^{217}Fr* nuclei. Also, because the range of energies is different for ^{215}Fr* as compared to ^{213,217}Fr* isotopes, the ΔR values at lower energies are obtained by extrapolating the fitted ΔR [21] values of ^{213,217}Fr* in respect of the data of Ref. [23].

For a complete and comprehensive analysis of the decay paths of all the three ^{213,215,217}Fr* isotopes, Fig. 1 shows the variation of ΔR with $E_{\rm c.m.}$, ranging from 71 to 94 MeV, for ER [Fig. 1(a)] and fission [Fig. 1(b)] processes, taking the deformed choice of decay fragments. The neck-length

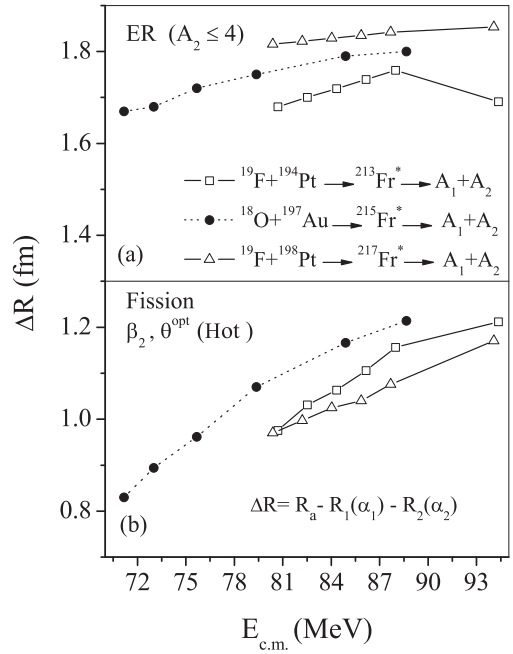

FIG. 1. Variation of neck-length parameter ΔR with $E_{\rm c.m.}$, obtained for (a) ER and (b) fission of compound systems ^{213,215,217}Fr*, for use of β_2-deformed decay products.

TABLE I. The characteristic properties like the neck-length parameter ΔR and maximum angular momentum ℓ_{max}, together with cross sections of channels contributing towards the evaporation residue (ER) cross section and the total ER cross section σ_{ER} predicted on the DCM for ^{215}Fr* compound nucleus formed in $^{18}O + ^{197}$Au reaction at various $E_{c.m.}$'s.

$E_{c.m.}$ (MeV)	E^*_{CN} (MeV)	T (MeV)	ℓ_{max} ($\hbar$)	ΔR (fm)	1n (mb)	2n (mb)	3n (mb)	^4H (mb)	σ_{ER}^{Total} (mb)
71.17	39.10	1.300	132	1.67	53.40	1.09	4.29×10^{-3}	3.24×10^{-2}	54.48
73.00	40.94	1.330	132	1.68	57.02	1.98	2.89×10^{-3}	1.67×10^{-2}	59.00
75.67	43.60	1.372	132	1.72	83.20	2.01	1.01×10^{-2}	1.13×10^{-1}	85.40
79.37	47.30	1.428	132	1.75	101.90	2.76	1.46×10^{-2}	3.60×10^{-4}	104.68
84.89	52.82	1.508	133	1.79	138.00	3.80	5.12×10^{-2}	3.02×10^{-4}	142.00
88.66	56.59	1.560	134	1.80	150.00	4.91	4.17×10^{-2}	6.20×10^{-4}	155.00

variations in Fig. 6 of Ref. [21] are used here to estimate the ΔR for evaporation residue path of ^{215}Fr*. For both the ER and fission processes, we notice a linear increase in ΔR with increase of $E_{c.m.}$, except at the highest one energy for ER in ^{213}Fr* system. Note that different ΔR's for the two processes of ER and ff mean that they occur in different time scales and evolve differently, subject to the nature of dynamics of compound nucleus formed. As expected from our earlier calculation for the ^{213,217}Fr* compound systems [21], the predicted ER channel for ^{215}Fr* requires larger ΔR in comparison to ff, as is depicted in Fig. 1 (compare two dotted lines), indicating that ER emission occurs earlier than the fission.

The above results are more explicitly given in Table I where the calculated contributions of ER cross-section and other parameters of the DCM are presented for ^{215}Fr* system only (for ^{213,217}Fr*, see Ref. [21]). It may be noted here that major contribution to total ER cross section in these calculations comes from mass 1 fragment, i.e., $1n$, contributing almost 97% of σ_{ER} for all the available energies. This happens because, in DCM, $1n$ channel is, in general, preformed strongly in CN [15], in comparison to other light particles in the exit channel. Also, it is important to note that, as compared to σ_{ER} here in Table I, our earlier calculations [22] resulted in a nearly negligible σ_{ER} for use of ΔR_{fiss}, i.e., from fits to fission cross sections. An experimental verification of the predicted σ_{ER} component in $^{18}O + ^{197}$Au reaction is thus called for.

Next, in view of our earlier work on ^{213,217}Fr* systems [21], we present here the results of our calculation on DCM for the data [26] available for the above said compound systems formed in $^{19}F + ^{194,198}$Pt reactions. Fission cross-section data are available at three higher energies [26], in addition to the ones reported by Mahata *et al*. [23] and used in Ref. [21], for the same two reactions. However, the ER contribution is missing in this recent data [26], contrary to the earlier measurements [23]. Since our earlier work [21] involved simultaneous fitting of both ER and fission cross sections, the same approach has been carried forward here for the present calculations. For this purpose, we extrapolated our previously obtained neck-length ΔR values in Fig. 1 for both the ER and fission processes in ^{213,217}Fr*. We observed that if we take ΔR values in the neighborhood of extrapolated ΔR's (within a variation of <0.1 fm), then the reported fission cross sections can be easily fitted within the DCM calculations. In other words, the data on fission cross sections [26] are nicely reproduced within the DCM approach for the extrapolated ΔR values within a certain variance of the order of 0.1 fm. These results are presented in Table II, together with the available experimental data and other calculated quantities and fitted parameters. Noting that, in the earlier experiment [23], a significant contribution of σ_{ER} is measured for both the compound systems ^{213,217}Fr*, and that σ_{ER} for ^{213}Fr* is relatively small, compared to ^{217}Fr*, at all measured energies, we find that the predictions of σ_{ER} at higher energies in Table II also support this result. Figure 2 depicts the complete result of our σ_{ER} and $\sigma_{fission}$ calculations for ^{213,217}Fr*, i.e., Fig. 5 of [21] extended to include the present calculations in reference to recent data [26] at three higher energies. We notice from Fig. 2 (and Table II) that DCM-based fission cross sections $\sigma_{fission}$ compare nicely with the experimental data [23,26] and the predicted ER

TABLE II. The DCM calculated fission cross sections consisting of asymmetric mass window $A_2 = 72$–94 for ^{213}Fr* and $A_2 = 78$–94 for ^{217}Fr* (plus their complementary fragments), compared with new experimental data [26] at higher three energies. Also tabulated are the predicted ER cross sections σ_{ER} along with other characteristic quantities.

$E_{c.m.}$	E^*_{CN}	T	ℓ_{max}	$\Delta R_{fission}$ (fm)		$\sigma_{fission}$ (mb)		ΔR_{ER} (fm)	σ_{ER} (mb)
(MeV)	(MeV)	(MeV)	($\hbar$)	Extrapolated	Fitted	DCM	Expt.	Extrapolated	DCM
				$^{19}F + ^{194}Pt \rightarrow ^{213}Fr^* \rightarrow A_1 + A_2$					
100.27	66.97	1.703	134	1.20	1.20	622	626	1.54	8.00
102.99	69.69	1.737	135	1.28	1.22	763	765	1.50	4.89
106.61	73.31	1.781	136	1.31	1.31	857	860	1.56	11.42
				$^{19}F + ^{198}Pt \rightarrow ^{217}Fr^* \rightarrow A_1 + A_2$					
97.40	60.50	1.605	135	1.21	1.16	371	378	1.87	216
102.80	65.89	1.674	136	1.29	1.11	523	523	1.89	229
106.56	69.65	1.720	138	1.35	1.20	660	670	1.87	241

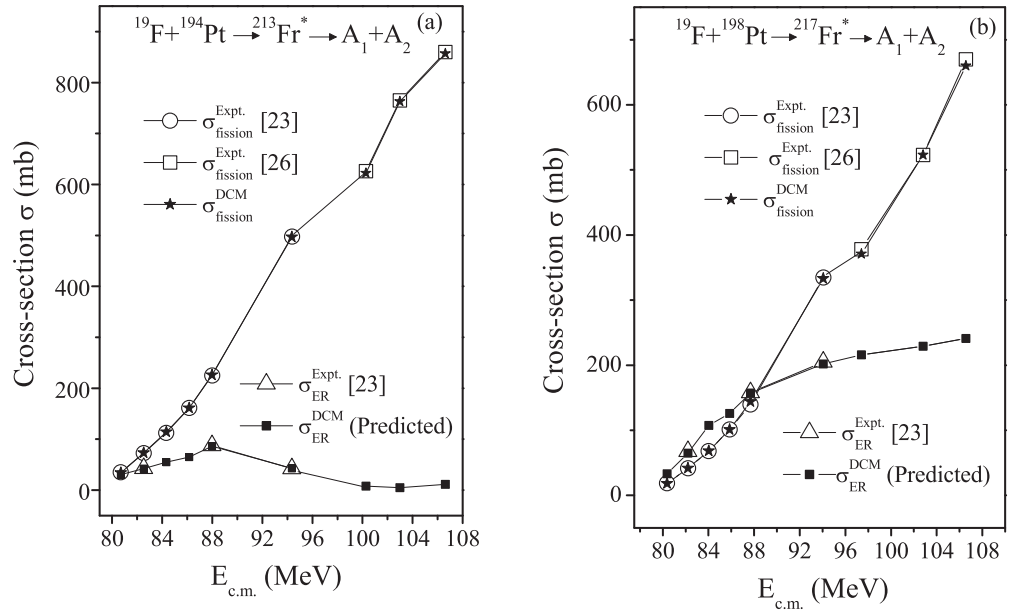

FIG. 2. Comparison of DCM-based calculated cross sections with the experimental data for ER and fission processes in (a) ^{213}Fr* and (b) ^{217}Fr* compound system. The figure is an extension of our previous work [21] to higher three energies in reference to new σ_{fission} data of Ref. [26] added to earlier data from Ref. [23]. σ_{ER} are also from Ref. [21], with predictions added for the highest three energies.

cross sections σ_{ER} at the highest three energies fit in to the systematics at lower energies for both the experiment and calculations [21,23]. An experimental verification of these predictions would be of further interest.

As a next step, we study the behavior of fission fragment anisotropy for the reactions $^{19}\text{F} + ^{194,198}\text{Pt}$ forming compound systems ^{213,217}Fr*, in order to check the consistency of results obtained earlier [22] for ^{215}Fr*. We first note that all the calculations presented above for ER and fission cross sections are performed for the sticking moment of inertia I_{S}, where the ℓ_{max} is fixed for $\sigma_{\text{LPs}} \to 0$. One may also notice that, as a result, the ℓ_{max} involved here in the reaction dynamics have much higher values, relative to ones for use of the nonsticking limit I_{NS}. Also, it has already been shown [18,22] that the limit I_{S} is more appropriate for obtaining fusion-fission cross sections, whereas I_{NS} is preferred for the fission anisotropy calculations.

Figures 3(a) and 3(b) and Table III show the variation of DCM-calculated fission fragment anisotropies within the SSPM approach [6] for the reactions $^{19}\text{F} + ^{194,198}\text{Pt}$, as a function of $E_{\text{c.m.}}$, compared with the experimental data [23].

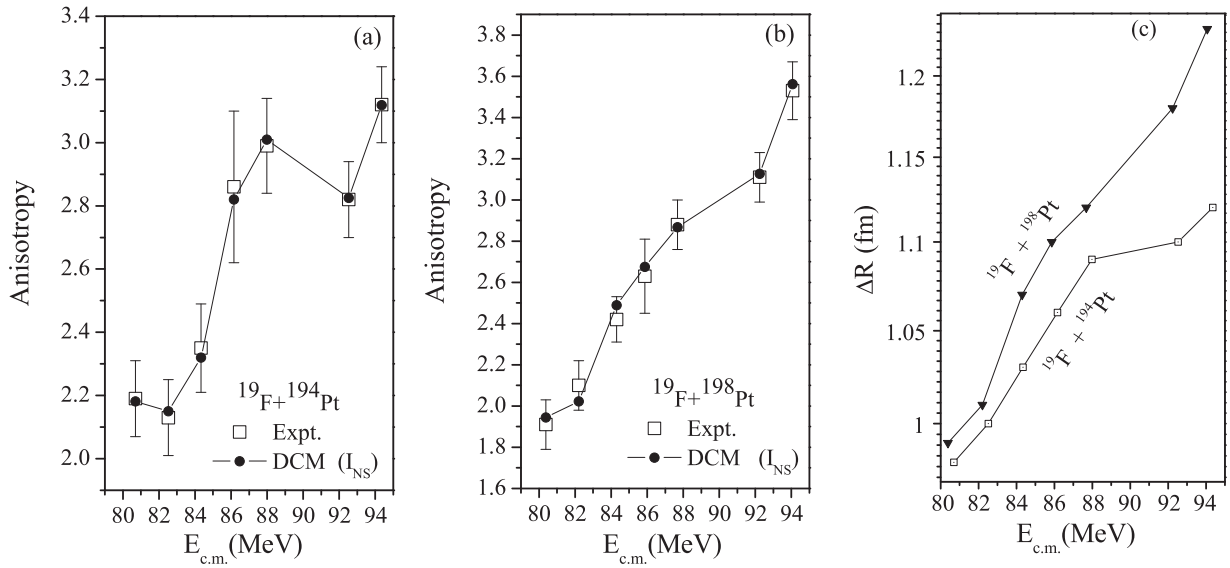

FIG. 3. The DCM calculated fission anisotropy, compared with the experimental data [23] for (a) $^{19}\text{F} + ^{194}\text{Pt}$ and (b)$^{19}\text{F} + ^{198}\text{Pt}$ reaction, using the nonsticking limit I_{NS} for moment of inertia. Panel (c) shows the anisotropy-fitted neck-length parameter ΔR for the same two reactions at various $E_{\text{c.m.}}$ values.

TABLE III. The fission anisotropies calculated within the use of the nonsticking limit of moment of inertia I_{NS} in the framework of DCM, for ^{213,217}Fr* compound systems formed in ^{19}F + ^{194,198}Pt reactions at various $E_{c.m.}$'s, compared with the experimental data [23].

$E_{c.m.}$	E^*_{CN}	T	ℓ_{max}	ΔR	Anisotropy A	
(MeV)	(MeV)	(MeV)	($\hbar$)	(fm)	DCM	Expt.
		^{19}F + ^{194}Pt → ^{213}Fr*				
80.69	47.39	1.436	24	0.98	2.18	2.19
82.51	49.21	1.463	24	1.00	2.15	2.13
84.34	51.04	1.489	26	1.03	2.32	2.35
86.16	52.86	1.515	32	1.06	2.82	2.86
87.98	54.68	1.541	33	1.09	3.01	2.99
92.53	59.23	1.603	33	1.10	2.82	2.82
94.35	61.05	1.627	34	1.12	3.11	3.12
		^{19}F + ^{198}Pt → ^{217}Fr*				
80.38	43.47	1.376	21	0.99	1.94	1.91
82.20	45.30	1.391	22	1.01	2.02	2.10
84.40	47.12	1.418	27	1.07	2.48	2.42
85.86	48.95	1.445	28	1.10	2.67	2.63
87.68	50.77	1.472	29	1.12	2.86	2.88
92.24	55.34	1.535	35	1.18	3.12	3.11
94.06	57.16	1.560	38	1.23	3.56	3.53

Interestingly, DCM calculated anisotropies for use of I_{NS} limit of moment of inertia give nice agreement with the data. In general, the experimental numbers for total angular momentum ℓ_{max} are based on the moment of inertia calculated by using the nonsticking ($I_{NS} = \mu R^2$) approach where the use of reduced mass alone corresponds to the supposition that the emission of fragment is prompt [14]. As a further check, we notice that the anisotropy-fitted ΔR, plotted in Fig. 3(c), for both the reaction channels, vary almost as a smooth function of $E_{c.m.}$, showing a similar behavior as in the case of fission (refer to Fig. 1). This simply means that the variation of ΔR with $E_{c.m.}$ is independent of the use of I_S or I_{NS}, and a closer look at Fig. 3 suggests that the neck-length parameter ΔR follows the variation pattern of fission fragment anisotropy.

Furthermore, we look at the values of ℓ_{max} presented in Table I of Ref. [21] and Table III here due to the use of sticking and nonsticking limits of moment of inertia. We find that, in ^{213,217}Fr* also, as a result of use of I_{NS} approximation, anisotropies are fitted at a much smaller ℓ_{max} values. This observation is consistent with the earlier result of Ref. [22] for ^{215}Fr*, which implies the fact that moment of inertia plays an important role regarding the dynamics involved in heavy-ion reactions.

Another quantity of interest is the variation of barrier modification parameter ΔV_B, plotted as a function of $E_{c.m.}$ in Fig. 4(a). This property of "barrier lowering" at sub-barrier energies is a built-in property of the DCM which has a direct dependence on the corresponding values of neck-length parameter (ΔR) used to fit the available data. It is relevant to mention here that ΔV_B is plotted for the decay of ^{213,215,217}Fr* to most probable fission fragments ^{128}Te + ^{85}Br, ^{130}Te + ^{85}Br, and ^{132}Te + ^{85}Br, respectively, for the deformed choice of fragments. It is observed from Fig. 4(a) that at a given $E_{c.m.}$ value, the barrier modification ΔV_B is least for ^{215}Fr* followed by ^{213}Fr* and ^{217}Fr*. No direct isospin (N/Z ratio) dependence on ΔV_B is observed, possibly due to the fact that ^{215}Fr* and ^{213,217}Fr* experiments were performed independently, over different ranges of energies. We have also calculated the ΔV_B at different ℓ values up to the ℓ_{max} in Fig. 4(b) for all the three reaction channels at $E^*_{CN} \sim 47$ MeV. We notice that

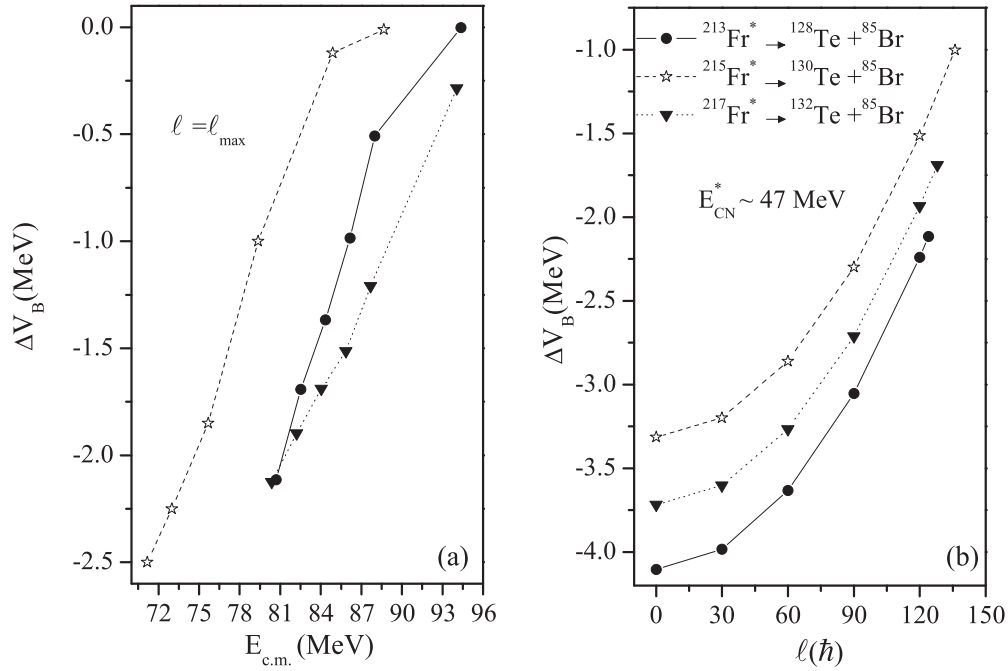

FIG. 4. (a) The barrier-lowering parameter ΔV_B as a function of $E_{c.m.}$ for the decay of ^{213,215,217}Fr* to most probable ^{128,130,132}Te + ^{85}Br fragments at $\ell = \ell_{max}$. (b) Variation of ΔV_B as a function of angular momentum ℓ ($\hbar$) at comparable $E^*_{CN} \sim 47$ MeV using β_2-deformed choice of fragments.

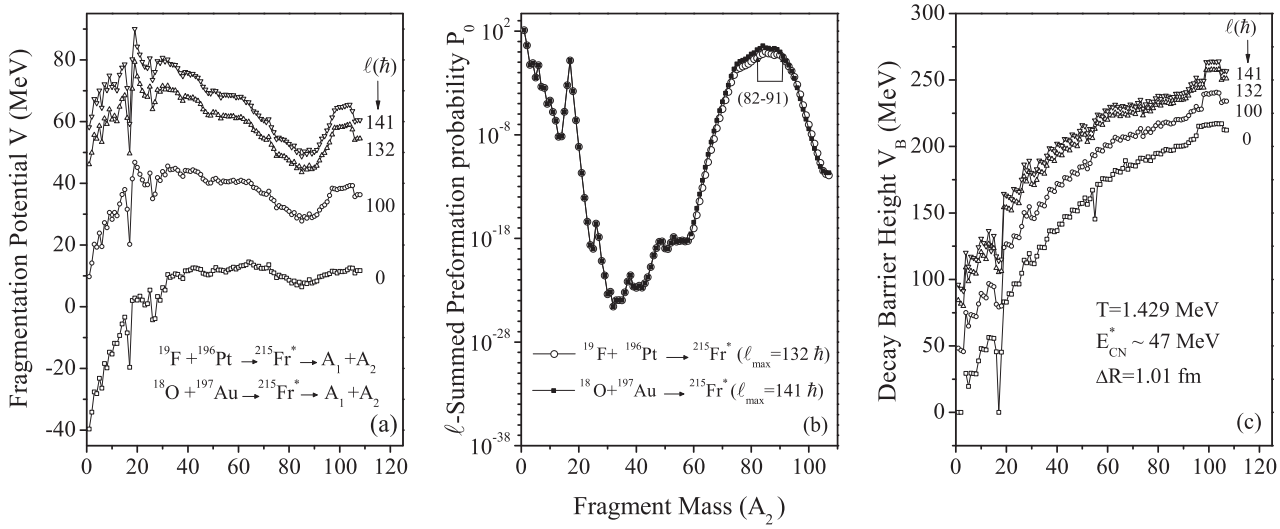

FIG. 5. (a) The variation of fragmentation potential as a function of light-fragment mass number A_2, at different ℓ values, for $^{19}F + ^{196}Pt$ ($\ell_{max} = 132\hbar$) and $^{18}O + ^{197}Au$ ($\ell_{max} = 141\hbar$) channels forming $^{215}Fr^*$ system at a comparable excitation energy. (b) The ℓ-summed fragment preformation probability P_0 plotted at ℓ_{max} values only for the two reactions. Panel (c) is same as for panel (a) but for the decay barrier height V_B.

ΔV_B keeps on increasing with a decrease in ℓ value and is observed to be least at higher angular momentum value. This observation clearly indicates the importance of ΔV_B at lower ℓ values, particularly in the below-barrier energy region.

Finally, we notice that the CN $^{215}Fr^*$ is formed in three different entrance channels [24,26], using ^{11}B, ^{18}O, and ^{19}F projectiles, whereas $^{213,217}Fr^*$ systems are due to ^{19}F-based reactions only [23]. Although a comparative analysis of ^{11}B and ^{18}O channels in the context of $^{215}Fr^*$ system was worked out in our earlier work [22] and here as we have addressed the reactions involving ^{19}F beam, it is also of interest to investigate the behavior of ^{19}F entrance channel in the context of $^{215}Fr^*$ nucleus. Therefore, in the following, we have made a comparative analysis of the decay of $^{215}Fr^*$ formed in $^{19}F + ^{196}Pt$ [26] and $^{18}O + ^{197}Au$ [22] reaction channels at a comparable excitation energy $E^*_{CN} \sim 47$ MeV ($T = 1.429$ MeV) in reference to available data. The variation of fragmentation potential $V(\eta)$, preformation probability P_0, and decay barrier height are investigated in order to reveal useful information about the dynamics involved in the reactions under consideration.

Figure 5(a) shows the variation of fragmentation potential for the decay of $^{215}Fr^*$ into various mass fragments at different ℓ values, in reference to the fission cross-section data [24,26] of $^{19}F + ^{196}Pt$ and $^{18}O + ^{197}Au$ reactions at $E^*_{CN} \sim 47$ MeV. Note that for both the reactions, DCM is found to consist of an asymmetric fission window, arising due to deformed (β_2) choice of fragments, where fragments in the mass range $A_2 =$ 82–91 (plus complementary heavy fragments) contribute toward fission process. This fission fragment window is same as was taken for comparative analysis of ^{11}B and ^{18}O channels in Ref. [22]. The ΔR values, obtained to fit the available data, were 0.96 and 1.07 fm [22], respectively, for the $^{19}F + ^{196}Pt$ and $^{18}O + ^{197}Au$ entrance channels. Since the two values are very close to each other, we have taken here an average of the two values, i.e., $\Delta R = 1.01$ fm, to fit the fission cross-section data. We notice from Fig. 5(a) that although the characteristic behavior of potential energy surfaces is different at lower versus higher ℓ values, the structure of the fragmentation potential does not change much in going from $\ell = 132\hbar$ (the ℓ_{max} value for $^{19}F + ^{196}Pt$) to $141\hbar$ (the ℓ_{max} value for $^{18}O + ^{197}Au$). This observation clearly indicates that the decay of $^{215}Fr^*$ is almost independent of the choice of entrance channel, like for ^{11}B and ^{18}O beams in Ref. [22]. At lower ℓ values, as expected, the contribution of ER is more prominent than the fission fragments, which otherwise start appearing only at higher ℓ values.

Based on the fragmentation potential in Fig. 5(a), we have depicted in Fig 5(b) the summed up preformation probability P_0 over ℓ values, as a function of light mass fragment A_2 for both the reaction channels at two different $E_{c.m.}$'s forming the same CN at about the same E^*_{CN} (~47 MeV). The ℓ-summed P_0 means the sum of probabilities of a fragment that is preborn in the CN prior to the decay process, over all contributing angular momentum states up to ℓ_{max}. It is relevant to mention here that, in the DCM, cross sections follow the trend of preformation probability P_0 [22], which means that structure effects are contained only in P_0. We find from Fig. 5(b) that the summed values of P_0 over ℓ are almost similar for both the reactions, which further indicates no significant signature of entrance channel effects.

To investigate further, we have plotted the barrier heights $V_B(A_2)$ at different ℓ's for the decay of $^{215}Fr^*$ formed in the same, above mentioned reaction channels in Fig. 5(c) using DCM. It is clear from this figure that V_B increases and hence the decay probability decreases with decrease in mass asymmetry, in agreement with the earlier calculations of Refs. [18,22] for the case of heavy nuclear system having fission as its prominent decay channel. On the other hand, the decay barrier heights almost overlap each other for $\ell_{max} = 132$ and $141\hbar$, i.e., independent of whether the compound nucleus $^{215}Fr^*$ is formed from $^{19}F + ^{196}Pt$ or $^{18}O + ^{197}Au$ entrance channels. In other words, the DCM-based calculations suggest

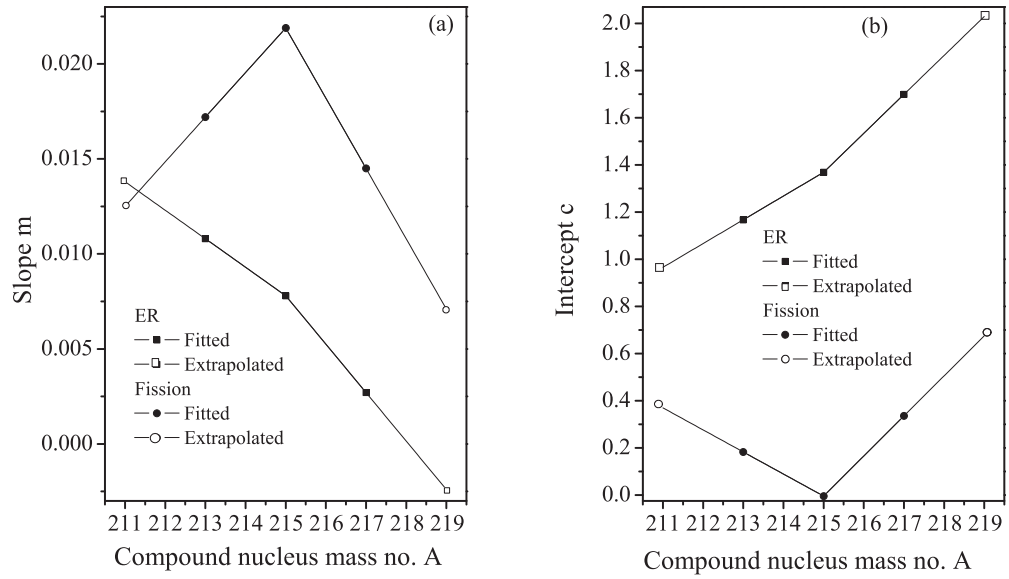

FIG. 6. (a) Slope and (b) intercept as a function of compound nucleus mass number A for straight-line fit of ΔR as a function of $E^*_{\rm CN}$. Filled symbols are fitted values and open symbols are extrapolated values.

that the decay of ^{215}Fr* is independent of the choice of entrance channel effects.

B. Role of shell effects in decay fragments of the Fr isotopes

In our earlier work [21], shell-closure effects of the decay fragments are shown to play an important role in the context of fragmentation process of ^{213,217}Fr* nuclei. In the present study we include the decay of ^{215}Fr*, as well as the two neighboring isotopes ^{211,219}Fr* formed in the proposed reactions ^{19}F + ^{192}Pt and ^{19}F + ^{200}Pt, in order to carry out a complete analysis of the possible shell effect of decay fragments or else the isospin (N/Z ratio) effects of various mass distributions and other characteristic quantities in $^{211-219}$Fr* isotopes.

First, we notice that in reference to experimental data [23, 24], the compound nucleus excitation energy $E^*_{\rm CN}$ is the same (∼47 MeV) for all the three ^{213,215,217}Fr* systems. Therefore, we carry out a comparative study of the decay mechanism of various odd-mass Fr isotopes at $E^*_{\rm CN} \sim 47$ MeV. In order to be able to predict the ER and fission cross sections for new isotopes ^{211}Fr* and ^{219}Fr*, we extrapolate the slope (m) and intercept (c) values obtained via straight line fits of the ΔR values of ^{213}Fr*, ^{215}Fr*, and ^{217}Fr* in Fig. 1, using

$$\Delta R = mE^*_{\rm CN} + c. \tag{14}$$

We obtain the straight line fits to both the ER and fission processes, in the following form of polynomials, for ^{213}Fr:

$$\Delta R^{\rm ER} = 0.0108E^*_{\rm CN} + 1.1674,$$
$$\Delta R^{\rm fission} = 0.0172E^*_{\rm CN} + 0.1826;$$

for ^{215}Fr:

$$\Delta R^{\rm ER} = 0.0078E^*_{\rm CN} + 1.369,$$
$$\Delta R^{\rm fission} = 0.0219E^*_{\rm CN} - 0.0044;$$

and for ^{217}Fr:

$$\Delta R^{\rm ER} = 0.0027E^*_{\rm CN} + 1.6992,$$
$$\Delta R^{\rm fission} = 0.0145E^*_{\rm CN} + 0.3354,$$

respectively.

Figure 6 shows a plot of the slope m [Fig. 6(a)] and intercept c [Fig. 6(b)], and their extracted values, for ER and fission fits obtained above, as a function of the CN mass number A. Here the filled symbols represent m and c values for ^{213,215,217}Fr* isotopes, and the open symbols represent the extrapolated values for ^{211,219}Fr* isotopes. Using the extrapolated values of m and c in Eq. (14), at the same $E^*_{\rm CN} \sim 47$ MeV, the neck length parameter ΔR is obtained and used in turn to calculate $\sigma_{\rm ER}$ and $\sigma_{\rm fission}$ for ^{211,219}Fr*. The results so obtained are given in Table IV, where one may see that the DCM predicts contributions of ER as well as fission cross sections for ^{211,219}Fr* rather small, compared to observed experimental data [23,24] for ^{213,215,217}Fr* isotopes.

Finally, we have calculated the fragment formation yields P_0, presented in Fig. 7, at the two extreme ℓ values for the decay of various isotopes of Fr at a similar excitation energy $E^*_{\rm CN} \sim$ 47 MeV in order to analyze the role of magic shells in mass distributions. The shell effects, in all the odd-mass Fr isotopes

TABLE IV. DCM-predicted evaporation residue cross sections ($\sigma_{\rm ER}$) and fission cross sections ($\sigma_{\rm fission}$) for ^{211,219}Fr* isotopes at the extrapolated ΔR values and common excitation energy $E^*_{\rm CN} \sim$ 47 MeV.

Compound nucleus	$E_{\rm c.m.}$ (MeV)	T (MeV)	$\ell_{\rm max}$ ($\hbar$)	$\Delta R_{\rm fiss}$ (fm)	$\sigma_{\rm fission}$ (mb)	$\Delta R_{\rm ER}$ (fm)	$\sigma_{\rm ER}$ (mb)
^{211}Fr*	81.84	1.437	118	0.95	22.93	1.61	5.06
^{219}Fr*	84.38	1.410	123	1.00	16.48	1.86	3.86

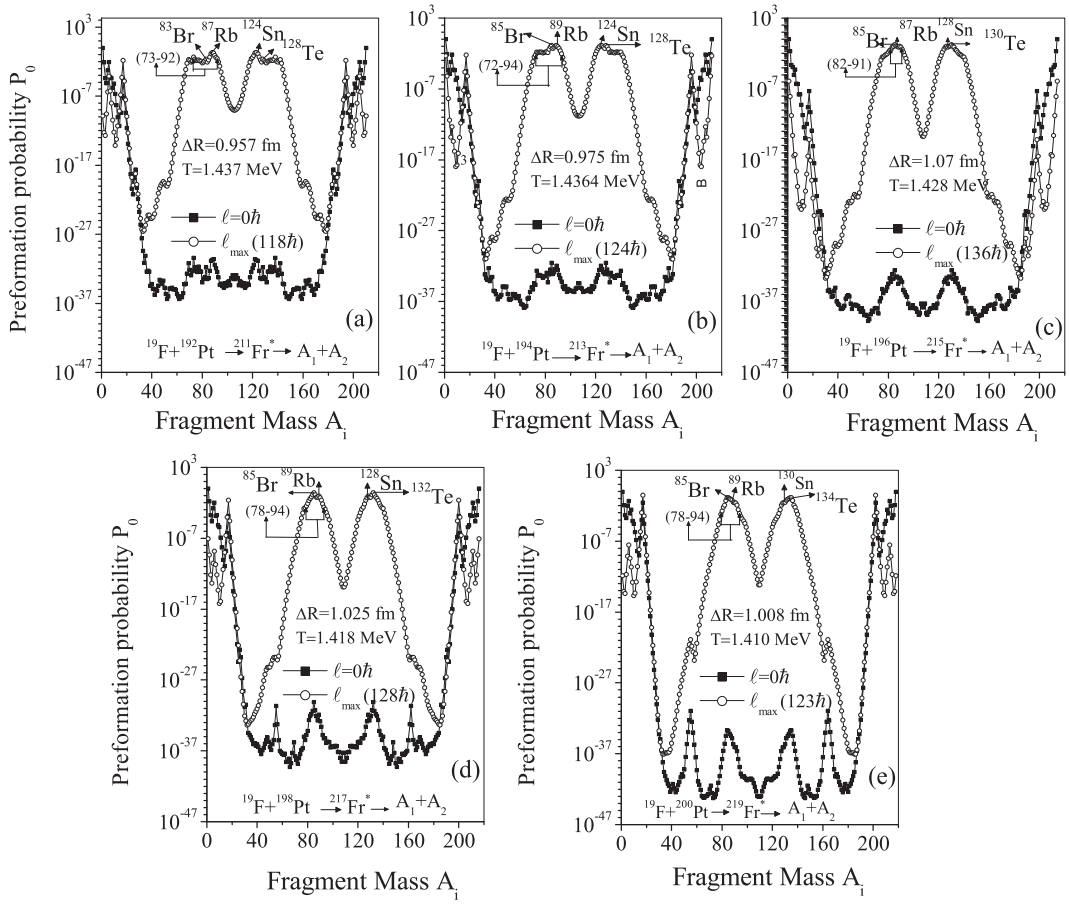

FIG. 7. Fragment preformation probability P_0 plotted as a function of fragment mass A_i ($i = 1, 2$) for different compound systems (a) ^{211}Fr*, (b) ^{213}Fr*, (c) ^{215}Fr*, (d) ^{217}Fr*, and (e) ^{219}Fr* at $E^*_{CN} \sim 47$ MeV, showing the presence of shell effects in all cases.

$^{211-219}$Fr*, arise due to the deformed closed shell around light-fragment charge $Z_2 = 36$ (actually at $Z_2 = 35$ and 37), and spherical shell closure around heavy-fragment charge $Z_1 = 50$ (actually at $Z_1 = 52$ and 50). This is explicitly marked in Fig. 7 in terms of two strong maxima (or, equivalently, double minima in Fig. 1 of fragmentation potential $V(A_2)$ in Ref. [21]) and as a hump or shoulder for both the light- and heavy-mass fragments. This hump seems to be a slightly more dominant for ^{211}Fr* (with neutron number $N = 124$) followed by ^{213}Fr* ($N = 126$) decay and goes on decreasing with the increase in N/Z ratio. The above observation enables us to conclude that shell closure effect of the decay fragments play an important role in all the above studied Fr isotopes.

It is relevant to mention here that the authors of experimental works [32,33] are interested in exploring the shell effects of compound nucleus ^{213}Fr*, an evident result of $N = 126$ magicity in this CN. However, the DCM allows us to study the shell effects in decay products only, and hence there is no way to study the role of magic proton or neutron numbers of the CN in this model. Another important observation is that for all the Fr isotopes studied here, the fission pattern remains the same, i.e., asymmetric, and the fragments in the mass range $A_2 =$ 72–94 seem to be contributing towards fission process. Note, however, that no individual fragments are identified in the available experiments [23,24]. Furthermore, it is generally believed that shell effects are washed away at higher excitation energies, which means that it will be of further interest to investigate the gradual variation of shell effects with the CN excitation energy.

IV. SUMMARY

Summarizing, we have extended our recent study [21,22] on the decay of odd-mass nuclear systems ^{213,217}Fr* formed in $^{19}\mathrm{F} + ^{194,198}\mathrm{Pt}$ reactions and ^{215}Fr* formed in $^{18}\mathrm{O} + ^{197}\mathrm{Au}$ (and more recently in $^{19}\mathrm{F} + ^{196}\mathrm{Pt}$) reaction in order to focus on the missing aspects of both the evaporation residue and fusion-fission processes, and the fission fragment anisotropies. The model used is the dynamical cluster-decay model (DCM), where effects of both the deformations and orientations of nuclei or fragments are included, with deformations taken up to β_2, and "optimum" orientations.

The ER cross sections are predicted for the ^{215}Fr* nucleus over a wide range of incident c.m. energy. In addition, we are able to account very well for the fission cross sections and predict the contribution of ER cross sections in reference to the latest data [26] available for ^{213,217}Fr* systems at higher three energies, in comparison to the earlier measurements of Mahata *et al.* [23]. Furthermore, in order to check the consistency of

our previous results for the decay of ^{215}Fr* [22], the work is extended to two different reaction channels, $^{19}\mathrm{F} + ^{196}\mathrm{Pt}$ and $^{18}\mathrm{O} + ^{197}\mathrm{Au}$. On comparing the results of calculations at a comparable excitation energy $E^*_{\mathrm{CN}} = 47$ MeV for the two reaction channels, it is observed that CN formation is independent of different entrance channels. The mass distributions of ^{211,213,215,217,219}Fr* are also worked out within the DCM, which clearly signifies the importance of shell effects of decay fragments in odd-mass Fr isotopes, supporting the result of our earlier work [21] for ^{213,217}Fr* isotopes.

ACKNOWLEDGMENTS

Financial support from the University Grants Commission (UGC), New Delhi, in the form of a Research Project and Dr. D. S. Kothari Grant is gratefully acknowledged.

[1] R. J. Charity, M. A. McMahan, G. J. Wozniak, R. J. McDonald, L. G. Moretto, D. G. Sarantites, L. G. Sobotka, G. Guarino, A. Pantaleo, F. Fiore, A. Gobbi, and K. D. Hildenbrand, Nucl. Phys. A **483**, 43 (1988).
[2] J. Gomez del Campo, R. L. Auble, J. R. Beene, M. L. Halbert, H. J. Kim, A. D'Onofrio, and J. L. Charvet, Phys. Rev. C **43**, 2689 (1991).
[3] S. J. Sanders, D. G. Kovar, B. B. Back, C. Beck, D. J. Henderson, R. V. F. Janssens, T. F. Wang, and B. D. Wilkins, Phys. Rev. C **40**, 2091 (1989).
[4] S. J. Sanders, Phys. Rev. C **44**, 2676 (1991).
[5] T. Matsuse, C. Beck, R. Nouicer, and D. Mahboub, Phys. Rev. C **55**, 1380 (1997).
[6] R. Vandenbosch and J. R. Huizenga, *Nuclear Fission* (Academic Press, New York, 1973).
[7] L. G. Moretto, Nucl. Phys. A **247**, 211 (1975).
[8] G. G. Adamian, N. V. Antonenko, W. Scheid, and V. V. Volkov, Nucl. Phys. A **633**, 409 (1998).
[9] V. I. Zagrebaev, Y. Aritomo, M. G. Itkis, Yu. Ts. Oganessian, and M. Ohta, Phys. Rev. C **65**, 014607 (2001).
[10] V. I. Zagrebaev, Yu. Ts. Oganessian, M. G. Itkis, and W. Greiner, Phys. Rev. C **73**, 031602(R) (2006).
[11] R. K. Gupta, M. Balasubramaniam, R. Kumar, N. Singh, M. Manhas, and W. Greiner, J. Phys. G: Nucl. Part. Phys. **31**, 631 (2005).
[12] R. K. Gupta, M. Balasubramaniam, R. Kumar, D. Singh, S. K. Arun, and W. Greiner, J. Phys. G: Nucl. Part. Phys. **32**, 345 (2006).
[13] R. K. Gupta, S. K. Arun, R. Kumar, and Niyti, Int. Rev. Phys. **2**, 369 (2008).
[14] B. B. Singh, M. K. Sharma, and R. K. Gupta, Phys. Rev. C **77**, 054613 (2008).
[15] S. K. Arun, R. Kumar, and R. K. Gupta, J. Phys. G: Nucl. Part. Phys. **36**, 085105 (2009).
[16] Niyti, R. K. Gupta, and W. Greiner, J. Phys. G: Nucl. Part. Phys. **37**, 115103 (2010); R. K. Gupta, Niyti, M. Manhas, and W. Greiner, *ibid.* **36**, 115105 (2009).
[17] M. K. Sharma, S. Kanwar, G. Sawhney, R. K. Gupta, and W. Greiner, J. Phys. G: Nucl. Part. Phys. **38**, 055104 (2011); D. Jain, R. Kumar, M. K. Sharma, and R. K. Gupta, Phys. Rev. C **85**, 024615 (2012).
[18] G. Sawhney, R. Kumar, and M. K. Sharma, Phys. Rev. C **86**, 034613 (2012).
[19] G. Sawhney and M. K. Sharma, Eur. Phys. J. A **48**, 57 (2012).
[20] M. Kaur, M. K. Sharma, and R. K. Gupta, Phys. Rev. C **86**, 064610 (2012).
[21] M. K. Sharma, S. Kanwar, G. Sawhney, and R. K. Gupta, Phys. Rev. C **85**, 064602 (2012).
[22] M. K. Sharma, G. Sawhney, R. K. Gupta, and W. Greiner, J. Phys. G: Nucl. Part. Phys. **38**, 105101 (2011); M. K. Sharma, G. Sawhney, S. Kanwar, and R. K. Gupta, Mod. Phys. Lett. A **25**, 2022 (2010).
[23] K. Mahata, S. Kailas, A. Shrivastava, A. Chatterjee, P. Singh, S. Santra, and B. S. Tomar, Phys. Rev. C **65**, 034613 (2002).
[24] S. Appannababu, S. Mukherjee, N. L. Singh, P. K. Rath, G. K. Kumar, R. G. Thomas, S. Santra, B. K. Nayak, A. Saxena, R. K. Choudhury, K. S. Golda, A. Jhingan, R. Kumar, P. Sugathan, and H. Singh, Phys. Rev. C **80**, 024603 (2009).
[25] V. S. Ramamurthy and S. S. Kapoor, Phys. Rev. Lett. **54**, 178 (1985).
[26] V. Singh, B. R. Behera, M. Kaur, A. Jhingan, P. Sugathan, D. Siwal, M. Oswal, S. Goyal, K. P. Singh, A. Saxena, and S. Kailas, in *Proceedings of the Department of Atomic Energy Symp. on Nucl. Phys.* **57**, 400 (2012); available on line at http://www.sympnp.org/proceedings/57/B6.pdf.
[27] N. J. Davidson, S. S. Hsiao, J. Markram, H. G. Miller, and Y. Tzeng, Nucl. Phys. A **570**, 61C (1994).
[28] W. D. Myers and W. J. Swiatecki, Nucl. Phys. **81**, 1 (1966).
[29] R. K. Gupta, N. Singh, and M. Manhas, Phys. Rev. C **70**, 034608 (2004).
[30] A. J. Sierk, Phys. Rev. C **33**, 2039 (1986).
[31] G. Royer and J. Mignen, J. Phys. G: Nucl. Part. Phys. **18**, 1781 (1992).
[32] V. Singh, B. R. Behera, M. Kaur, P. Sugathan, K. S. Golda, A. Jhingan, J. Sadhukhan, D. Siwal, S. Goyal, S. Santra, A. Kumar, R. K. Bhowmik, M. B. Chatterjee, A. Saxena, S. Pal, and S. Kailas, Phys. Rev. C **86**, 014609 (2012).
[33] V. Singh, B. R. Behera, M. Kaur, A. Kumar, P. Sugathan, K. S. Golda, A. Jhingan, M. B. Chatterjee, R. K. Bhowmik, D. Siwal, S. Goyal, J. Sadhukhan, S. Pal, A. Saxena, S. Santra, and S. Kailas, Phys. Rev. C **87**, 064601 (2013).